HHS Public Access

Author manuscript

Biomaterials. Author manuscript; available in PMC 2022 September 01.

Published in final edited form as:

Biomaterials. 2021 September ; 276: 120995. doi:10.1016/j.biomaterials.2021.120995.

Functionalized 3D-printed silk-hydroxyapatite scaffolds for enhanced bone regeneration with innervation and vascularization

Vincent Fitzpatrick, **Zaira Martin Moldes**, **Anna Deck**, **Ruben Torres-Sanchez**, **Anne Valat**, **Dana Cairns**, **Chunmei Li**, **David L. Kaplan***

Department of Biomedical Engineering, Tufts University, Medford, MA, 02155

Abstract

Our goal was to generate functionalized 3D-printed scaffolds for bone regeneration using silk-hydroxyapatite bone cements and osteoinductive, proangiogenic and neurotrophic growth factors or morphogens for accelerated bone formation. 3D printing was utilized to generate macroporous scaffolds with controlled geometries and architectures that promote osseointegration. We build on the knowledge that the osteoinductive factor Bone Morphogenetic Protein-2 (BMP2) can also positively impact vascularization, Vascular Endothelial Growth Factor (VEGF) can impact osteoblastic differentiation, and that Neural Growth Factor (NGF)-mediated signaling can influence bone regeneration. We assessed functions on the 3D printed construct via the osteogenic differentiation of human mesenchymal stem cells; migration and proliferation of human umbilical vein endothelial cells; and proliferation of human induced neural stem cells. The scaffolds provided mechanical properties suitable for bone and the materials were cytocompatible, osteoconductive and maintained the activity of the morphogens and cytokines. Synergistic outcomes between BMP-2, VEGF and NGF in terms of osteoblastic differentiation in vitro were identified, based on the upregulation of genes associated with osteoblastic differentiation (Runt-related transcription factor-2, Osteopontin, Bone Sialoprotein). Additional studies will be required to assess these scaffold designs in vivo. These results are expected to have a strong impact in bone regeneration in dental, oral and maxillofacial surgery.

*Corresponding Author.

Vincent Fitzpatrick: Conceptualization, Methodology, Software, Validation, Formal analysis, Investigation, Data Curation, Writing - Original Draft preparation, Visualization, Project administration; **Zaira Martin Moldes**: Validation, Formal analysis, Investigation, Data Curation, Writing - Original Draft preparation, Writing - Review & Editing, Visualization; **Anna Deck**: Investigation, Writing - Original Draft preparation Writing - Review & Editing; **Ruben Torres-Sanchez**: Investigation, Writing - Review & Editing; **Anne Valat**: Investigation, Writing - Review & Editing; **Dana Cairns**: Resources; **Chunmei Li**: Investigation, Writing - Review & Editing, Visualization, Supervision; **David L. Kaplan**: Conceptualization, Writing - Review & Editing, Supervision, Funding acquisition

Competing interests

The authors have no competing interest to declare.

Declaration of interests

The authors declare that they have no known competing financial interests or personal relationships that could have appeared to influence the work reported in this paper.

Keywords

3D printing; silk; bone regeneration; tissue engineering; vascularization; innervation

Introduction

Bone is a dynamic, innervated and vascularized tissue, with an inherent ability to regenerate after injury. As such, most fractures or defects require minimal intervention to fully recover. However, severe cases of bone loss may not heal spontaneously. These critical-size defects can be the result of bone tumor resection, infection, severe trauma or even development deformities, and require a surgical approach to restore bone volume [1]. The treatment of these defects using bone substitutes is increasingly common, with bone grafting representing over two million procedures yearly worldwide [2]. Current methods of acquiring bone for these types of surgeries include autografts (gold standard), allografts, and xenografts. Autografts and allografts are both limited by issues of donor tissue availability and donor site morbidity, while both allografts and xenografts present issues with cost and disease transmission [3]. These issues have driven research into new, cost-effective methods to treat these defects, using a tissue engineering approach [4]. By combining new biomaterials, better physicochemical properties, morphogen presentation and even cell therapy, this strategy offers a promising solution to the shortage of available tissue and the potential to regenerate even critically sized bone defects.

Implant success in bone tissue engineering requires materials and processes that promote osseointegration. This functional connection between implanted material and living bone is dependent on: (1) a match between the topography of the implant and the recipient site [5]; (2) adequate porosity for new bone growth [6]; (3) mechanical properties consistent with the surrounding native bone [7]; (4) cytocompatiblity and biocompatibility of the material; (5) osteoconductivity of the implant [8]; (6) osteoinduction by the implanted material [8]. Current clinically relevant biomaterials used for bone tissue engineering include bone blocks, bone chips, and bone cements [9]. Bone blocks are preformed cubical shaped structures that offer controllable porosity yet require the surgeon to trim the part to match the patient’s anatomy, resulting in longer operative times. Bone chips are pieces of morselized cortical-cancellous bone that offer good porosity, but confer limited mechanical strength and poor osseointegration [10]. Finally, bone cements are quick-setting pastes that are moldable and can be customized to the patient’s anatomy, but usually present low porosity [11]. 3D printing is an emergent and promising technique that could provide a solution to all of the limitations. This approach can be used to generate bespoke, microporous biomaterial constructs with customizable structure and mechanical properties. Unlike the other techniques described, 3D printing can closely mimic the internal architecture of bones by recreating hierarchical structures like Haversian canals [12]. In the context of biomedical engineering, 3D printing encompasses additive manufacturing techniques allowing the fabrication of three-dimensional constructs through the layer-by-layer deposition of a bone cement. Bone cements used for bone tissue engineering need to be biocompatible, osteoconductive/osteoinductive, degradable, and have mechanical properties close to the surrounding bone to provide mechanical support [13].

Silk fibroin protein has been extensively used for tissue engineering applications, including bone scaffolds, due to its tunable mechanical strength and flexibility, biocompatibility, and osseointegration [14–26]. Silk materials do not trigger significant inflammation or immunological reactions, and their degradation rate can be tuned depending on the desired application [27]. Further, silk can be used as a drug delivery vehicle for enzymes, growth factors, and antibiotics, allowing its biofunctionalization [28–32]. By combining calcium phosphate hydroxyapatite with silk, the properties of silk can be utilized with a chemical composition and mechanical properties closer to that of native bone. Indeed, hydroxyapatite is the major inorganic portion of bone, and is commonly used in orthopedic and dental materials, so its biological effects are well-established [33]. Thus, hydroxyapatite meets the need for a biocompatible and osteoinductive component while also improving the mechanical strength of composite scaffolds when added to a polymer matrix [34].

Functionalization of a material for bone regeneration can greatly improve the properties of an otherwise passive material. Current strategies for functionalization described in the literature focus on osteoinduction, most commonly using growth factors and morphogens like Bone Morphogenetic Protein-2 (BMP2) [35,36], or nanoparticles like bioactive glass [37] or strontium [38]. However, bone is a complex, multi-component, and highly dynamic tissue, with blood vessels and nerves which form a network within the mineralized tissue and also play a key role in bone tissue functions. Past strategies for bone repair and regeneration mostly ignored this multi-component approach, while in the past decade bone repair strategies have shifted toward including the invasion of blood vessels [39–41], and even more recently to actively encouraging vascularization using bioactive molecules like Vascular Endothelial Growth Factor (VEGF) [42–44]. However, aside from vascularization, there is also strong evidence for the importance of nerves in bone repair [45–48], yet no bone repair strategies that integrate innervation have been reported. Thus, building neurovascularized networks within bone scaffolds is hypothesized to improve the regeneration of bone tissue, resulting in more rapid and higher quality bone tissue outcomes. The importance of such synergies in bone-related outcomes is evidenced by the reduced the numbers of sensory fibers, blunted revascularization, and delayed ossification of the fracture callus when Nerve Growth Factor (NGF) pathways are inhibited in mice [49].

In this study, we developed a silk/hydroxyapatite bone cement for the 3D printing of customizable scaffolds for bone engineering. To validate the potential of this bone cement as a biomaterial for bone tissue engineering, the mechanical properties, architecture and microporosity were characterized. We further investigated biological relevance by studying the ability of these constructs to sustain the adhesion, growth, proliferation and differentiation of human mesenchymal stem cells *in vitro*. Finally, we functionalized the bone cement using growth factors and morphogens promoting osteoinduction (BMP2), vascularization (VEGF) and innervation (NGF). The bioactivity of these factors in the 3D printed constructs was evaluated in vitro through osteogenic differentiation of human mesenchymal stem cells; migration and proliferation of human umbilical vein endothelial cells; and proliferation and neurite extension of human induced neural stem cells. These specific cell responses are key steps towards the development of this next generation of functionalized, 3D printed bone scaffolding to promote multicellular responses in the context of bone tissue system regeneration.

Materials and Methods

Silk preparation:

The silk solution used for bone cement preparation was prepared as described in our published protocol [96]. Briefly, pieces of *Bombyx mori* cocoons were boiled for 60 minutes in 0.02 M aqueous Na_2CO_3, then rinsed extensively in diH_2O and dried overnight. The dry silk fibroin was dissolved in 9.3 M aqueous LiBr solution at 60°C for 4 hours. The silk/LiBr solution was dialyzed against distilled water for 2 days, with 10 water changes. The solution was centrifuged at 9,000 rpm at 4°C twice for 20 min. The unconcentrated solution was then concentrated in dialysis cassettes at room temperature until a concentration of 25–30% was reached. The concentration of the silk solution was determined by calculating the weight ratio between the wet and dry solution.

Bone cement preparation and printing:

The bone cements were prepared by mixing hydroxyapatite (HAP) with diH_2O and concentrated silk solution. The liquid-to-powder ratio was optimized to 1.2:1 (v/w), which produced an easily extrudable bone cement. The three components (silk, HAP, water) of the bone cements were mixed sequentially using two syringes connected by a luer lock connector, until a paste was obtained. This paste was extruded through a 23Ga 1/2-inch blunt needle (McMaster Carr), using a homemade paste extrusion 3D printer to generate scaffolds with controlled geometry and macroporosity. The 3D printer was built in our lab, and the stepper motors used for the movement of the stage in the x and y directions, the movement of the printhead in the z direction and the extrusion were controlled by an Arduino board running the Marlin firmware. The software used to control the 3D printer was Repetier, layer height was set at 410 μm, and for the cell culture studies the porosity was set to 30%, for the formation of larger macropores. Scaffolds were dried in an environmental controller at 95% humidity and 37°C overnight; they were sterilized by autoclaving prior to cell culture.

For the “printed” conditions, BMP2 (355-BM-010, R&D Systems), VEGF (100–20, Peprotech) and NGF (256-GF-100, R&D systems) were loaded into the bone cement by adding the bioactive molecule to the aqueous component prior to mixing. The morphogens were loaded into the constructs in order to obtain 1 μg of morphogen per construct. All subsequent steps except for sterilization were the same as for the unloaded constructs. Sterilization was achieved by placing the constructs for 30 minutes in an ethanol-saturated environment, at 37°C, followed by 20 minutes under the UV light.

For the “soaked” conditions, BMP2, VEGF and NGF were loaded into autoclaved (for sterilization) constructs under aseptic conditions, in a biosafety cabinet. A volume of 100 μL of morphogen solution containing 1 μg of BMP2, VEGF or NGF was deposited onto the surface of the 3D printed construct and allowed to absorb into the construct until fully dry (~45 min). *Uniaxial compression testing:* Uniaxial compression tests were carried out on an Instron 3366 machine (Instron, Norwood, USA) using ambient conditions, in accordance with conditions detailed in ASTM F451 (Standard Specification for Acrylic Bone Cement). The loading rate was 20 mm/min. A 1 kN load cell was used, and the test specimens were cylinders 12 mm high and 6 mm in diameter,. Multiple samples (n = 5) were tested for

each condition. For conditions labeled “wet”, the samples were completely submerged in phosphate-buffered saline (PBS) at 37°C for 1 hour prior to testing.

FTIR:

FTIR spectra were gathered utilizing FT/IR-6200 Spectrometer (Jasco, USA), equipped with a triglycine sulfate detector in attenuated total reflection (ATR) mode. The measurements were taken in the range of 4000–400 cm^{-1} at a resolution of 2 cm^{-1} with 128 scans. The background spectra were collected under the same conditions and subtracted from the scan for each sample.

Growth factor release study:

Enzyme-linked immunosorbent assay (ELISA) was performed to analyze the release of the growth factors over time. Unloaded scaffolds (Control) and scaffolds loaded with 1 μg of either BMP-2, VEGF or NGF, or the three factors together during (Printed) or after (Soaked) the 3D-printing process were immersed in 2 ml of Phosphate Buffered Saline (PBS) pH 7.4 and incubated at 37°C. After 1h, 3h, 6h, 12h, 1, 3, 5 and 7d 100 μl samples was taken and replaced with fresh PBS. A commercially available sandwich ELISA kit based on a human BMP-2 (Human BMP-2 DuoSet ELISA, DY355), human VEGF (Human VEGF DuoSet ELISA, DY293B) and human NGF (Human NGF DuoSet ELISA, DY256) antibody-coated plate (all purchased from R&D Systems, Minneapolis, MN, US) were utilized. The ELISA assay was performed using Nunc-Immuno™ MaxiSorp™ (Nalge Nunc International Corporation, Rochester, NY, US) plates that were coated with anti-human BMP-2, VEGF or NGF monoclonal antibody prepared in PBS and incubated overnight at room temperature, with the protocol performed following the manufactureŕs instructions. ELISA plates were then washed 3× and blocked with 0.5% bovine serum albumin (BSA) in PBS for 1–3 hours at room temperature. After washing again (3×), standards, controls and cell supernatant were added to the ELISA plates and incubated at room temperature for approximately 2 hours. The ELISA plates were then washed 3× and detection antibody was added and incubated overnight at 4°C. The plates were washed 3x and Streptavidin-HRP conjugate was added to the wells, incubated for 20 minutes at room temperature and subsequently washed 4×. The TMB substrate was then added to the wells and plates were incubated an additional 20 minutes at room temperature while protected from light. The reaction was stopped using 2 N sulfuric acid. Sample absorbance was read at 450 and 570 nm on a microplate spectrophotometer (Molecular Devices, Sunnyvale, CA). Standard curve analysis was performed using a 4-parameter logistical fit.

Cell culture on 3D printed scaffolds:

Human mesenchymal stem cells (hMSCs) were isolated from total bone marrow aspirate from a healthy, non-smoking male under the age of 25 (Lonza, USA). After isolation, the hMSCs were allowed to reach 80% confluence, after which they were trypsinized, suspended in FBS containing 10% DMSO and stored in liquid nitrogen. hMSCs (passage number < 5) were seeded into the 3D printed constructs, in a 24-well plate, using 1 mL of cell suspension with a density of 400 x 10^3 cells/mL. For conditions on tissue culture polystyrene, a cell seeding density of 10 x 10^3 was used. After seeding, the constructs were left in growth medium (DMEM high glucose GLUTAMAX (Gibco), 10% Fetal Bovine

Serum (Gibco), 1% antibiotic-antimycotic (Gibco), 1% Non-Essential Amino Acids (Gibco) and 5 ng/mL basic fibroblast growth factor (Gibco)). After 2 days the growth medium was replaced with either fresh growth medium or with osteogenic medium and changed every 2–3 days for the duration of the study. Osteogenic medium consisted of DMEM high glucose GLUTAMAX (Gibco), 10% Fetal Bovine Serum (Gibco), 1% antibiotic-antimycotic (Gibco), 100 nM dexamethasone (Sigma-Aldrich), 10 mM sodium β-glycerophosphate (Sigma-Aldrich), and 0.05 mM L-ascorbic acid. For the qPCR study, hMSCs were seeded at a density of 1.2 x 10^6 cells per construct in 1 mL, allowed to adhere for 6–8 hours and then switched to osteogenic medium. Medium was changed every 2–3 days.

Metabolism:

The metabolic activity of cells was determined by incubating cells with alamarBlue at 2, 7, 14, 21, 28 and 35 days, according to the manufacturer's instructions. Briefly, 100 μm of alamarBlue was added to each well, left to incubate for three hours. The medium was then collected, and the fluorescence was measured using a microplate reader (excitation: 560 nm; emission: 590 nm).

Cell staining:

For each time point, the constructs were rinsed with PBS, and cells were fixed using a 4% formaldehyde solution, permeabilized with 0.2% Triton X-100 in PBS and blocked with 2% BSA in PBS. Actin was labeled with Phalloidin–Tetramethylrhodamine B isothiocyanate (Sigma) and nuclei were stained with DAPI (Sigma). Osteopontin (OPN) was stained using a rabbit anti-osteopontin primary antibody (1/1000, ab8448, Abcam), secondary antibody goat anti-rabbit 594 (1/500, A11072, Thermofisher).

Osteogenic differentiation measurement:

ALP staining was carried out after 21 days of culture in growth or osteogenic medium, using nitro-blue tetrazolium chloride (NBT)/ 5-bromo-4-chloro-3'-indolyphosphate p-toluidine salt (BCIP) Alkaline Phosphatase Substrate (Sigma), according to the manufacturer's instructions. The combination of NBT and BCIP yields an intense, insoluble black-purple precipitate when reacted with alkaline phosphatase. ALP enzymatic activity was determined after 21 days of culture in either growth or osteogenic medium. Briefly, cells were lysed with 0.1% Triton X100 in PBS, followed by sonication for 5 seconds at 20% intensity. ALP activity was measured using the Alkaline Phosphatase Assay Kit (Abcam), according to the manufacturer's instructions. Absorbance was measured at 405 nm using a microplate reader. ALP activity was normalized to protein content, using a Pierce BCA Protein Assay Kit (Thermofisher), carried out on the same lysate as for ALP activity quantification. Absorbance was measured at 562 nm.

HUVEC culture:

Normal Human Umbilical Vein Endothelial Cells (HUVEC, passage <10, Lonza) were cultured in Endothelial Growth Medium (EGM-MV, Lonza). They were passaged using 0.25% trypsin-EDTA solution (Gibco) when they reached 80–90% confluence. For the migration assay, the cell culture inserts were placed into the wells of the 24-well plate. The

inserts were first coated on both sides with 0.1% gelatin solution at 37°C for one hour, then rinsed with PBS. Then 750 μL of medium was added to the outer compartment of each well. A total of 50,000 HUVECs were seeded into each cell culture insert the 24-well plates and incubated in a humidified incubator (37°C, 5% CO_2) for 3 hours. The cells were then fixed and stained with phalloidin and DAPI. For proliferation, 50,000 HUVECs per construct were seeded on the constructs and kept in culture for 7 days. Medium was changed every 2–3 days and at days 3 and 7, 10% alamarBlue was added to each well and incubated for 3 hours. The medium was then collected, and the fluorescence was measured using a microplate reader (excitation: 560 nm; emission: 590 nm).

hiNSC culture:

hiNSCs were produced as previously described[51]. hiNSCs were seeded at a density of 750 x 10^3 cells per construct and cultured in KO medium for the duration of the study. At day 7, 10% alamarBlue was added to the well and incubated for 3 hours. The medium was then collected, and the fluorescence was measured using a microplate reader (excitation: 560 nm; emission: 590 nm).

Microscopy:

Bright-field and fluorescent images were obtained using a Keyence BZ-X700 microscope and associated software. Fluorescent images of 3D samples were obtained using a Leica TCS FLIM SP8 (Wetzlar, Germany) confocal microscope. Scanning electron microscopy (SEM) was performed using a Zeiss Evo MA10 (Carl Zeiss Microscopy, Germany) to visualize the morphological features, including the microporosity, of the 3D printed construct. After fixation, cells and constructs were dried in ethanol baths of increasing concentration, followed by hexamethyldisilazane (HMDS, Sigma). The constructs were then cut in half using a scalpel and gold-sputter–coated for analysis. The measurement of pores and filaments was carried out using the SEM micrographs of multiple 3D printed constructs, picking random features and measuring using ImageJ.

RNA isolation and quantitative reverse transcriptase real-time polymerase chain reaction (qRTPCR)

Total RNA was extracted from 3-day and 7-day cultures using RNeasy Mini kit (QIAGEN, Hilde, Germany). RNA samples were then DNase I-treated using the TURBO DNA-free Kit according to the manufacturer's instructions (Invitrogen, Carlsbad, CA, USA). The concentration and purity of the RNA samples were assessed using a Nanodrop™ 2000 (Thermo Scientific, Carlsbad, CA, USA). Synthesis of total cDNA was performed using the Transcriptor First Strand cDNA Synthesis kit (Roche Diagnostics, Basel, Switzerland) in 20-μL reactions containing 150 ng of total RNA, 1 μM concentration of each dNTP, 10 units of reverse transcriptase, 20 units of Protector RNase Inhibitor, and 60 μM random hexamers, provided by the manufacturer. Samples were incubated at 25°C for 10 min and then at 55°C for 30 min. Reactions were terminated by incubation at 85°C for 5 min. Real-time PCR assays were performed in a CFX96 Deep Well Real-Time PCR System (Bio-Rad Laboratories, Hercules, CA, USA). The cDNA samples were analyzed for gene expression relative to the GAPDH housekeeping gene using LightCycler® 480 SYBR Green I Master (Roche Diagnostics, Basel, Switzerland). PCR amplifications were carried out with one

denaturation cycle (95°C for 10 min), followed by 50 cycles of amplification (95°C for 10 s, 60°C for 10 s, and 72°C for 10 s). After amplification, melting curves were generated to confirm amplification of a single product. All primers used to amplify transcripts from target genes, are listed in Table 1. Expression of these genes was compared with control samples cultured in the absence of growth factors (TCP). For each sample, the Ct value was defined as the cycle number at which the amplification of each target gene was in the linear range of the reaction. Relative expression levels for each gene were calculated by normalizing to the Ct value of GAPDH housekeeping gene and to the normalized level of the control sample ($2^{-\Delta\Delta Ct}$)[52]. The analysis was performed in two technical replicates from five biological samples.

Sintering:

Isothermal sintering was carried out in a Lindberg/Blue M Tube Furnace (ThermoFisher). A temperature ramp of 10°C/min was applied, until the furnace reached a temperature of 1,100°C, followed by a dwell time of 3 hours. The constructs were then allowed to cool to room temperature.

Statistics:

The results were analyzed on GraphPad Prism, using unpaired t tests or ordinary one-way ANOVA, where appropriate. A p-value of 0.05 or lower was considered as statistically significant. The number of asterisks on the graphs represent the following levels of significance: * $P \leq 0.05$; ** $P \leq 0.01$; *** $P \leq 0.001$; **** $P \leq 0.0001$.

Results

1. Characterization of the Silk/HAP bone cements and scaffolds

Silk solution and hydroxyapatite powder were mixed at room temperature, resulting in a thick, homogeneous, paste-like bone cement. The hydroxyapatite powder used had a particle size ranging from 0.5 to 10 μm, with certain aggregates reaching several tens of μm (Fig. 1.c, right). This bone cement could be steadily extruded out of a 5 mL syringe (Beckton Dickinson) and through a 23Ga, ½-inch nozzle. By mounting the syringe on a homemade paste extrusion 3D printer, we were able to control the extrusion rate of the paste, allowing the formation of regular filaments with a diameter of ~450 μm (Fig 1.a and 1.c). The paste extrusion printer allowed us to deposit these filaments with a resolution of ~350 μm. Further, we could stack these filaments vertically at the centimeter scale, generating 3D printed constructs with controlled macroporosity and with regular filament deposition and interconnected pores throughout (Fig. 1.a and 1.d). Once printed, the constructs were placed in an environment with 95% humidity, to ensure slow setting and to prevent cracking of the constructs during setting. Setting was the drying of the construct from the paste to a solid state, accompanied by a transition of the silk protein structure from random coil/helix structure to beta-sheet, as assessed by FTIR (Fig. 1.f). The mechanism of this change in molecular structure of the silk fibroin has previously been described [53]. The molecular conformation of silk fibroin is characterized by β-sheet absorption peaks at around 1630 cm^{-1} and random coil conformation absorption peaks at 1650 cm^{-1}. After setting, the filaments did not display any visible cracks, and the surface of the filaments

appeared smooth at lower magnifications (~50X) by scanning electron microscopy (SEM) (Fig. 1.c, left). Higher magnification (>100X) confirmed the absence of cracks and revealed the presence of small pores with a diameter of approximately ~10 μm over the entire surface of the dried constructs (Fig 1.c, center). To evaluate the use of the bone cement for printing larger, centimeter-scale constructs with more complex geometries, a miniaturized model of a femur, vertebra, and a mandible were successfully printed (Fig 1.b). Uniaxial compression tests were carried out to assess the effect of silk incorporation on the mechanical properties of the constructs. The compressive strength of the dried HAP/water mixture without silk was 2.42 ± 0.75 MPa (Fig. 1.g). The presence of silk significantly improved the mechanical properties of the constructs, with the average compressive strength of the dry constructs with 5%, 10% and 15% silk increasing to 19.64 ± 2.70 MPa, 19.41 ± 3.82 MPa and 48.74 ± 7.76 MPa, respectively. The composition and mechanical properties were further altered by applying post-printing sintering. By heating the constructs to 1,100°C for 3 hours, the compressive strength was 5.11 ± 2.24 MPa, 11.20 ± 6.14 MPa, 15.38 ± 5.04 MPa and 20.29 MPa ± 9.71 MPa for the 0%, 5%, 10% and 15% silk constructs, respectively. This step also led to shrinking of the constructs of 20.62 ± 5.87%, 39.29 ± 2.94%, 40.96 ± 3.17% and 42.45 ± 3.81%, respectively (Fig. 1.e). In an environment mimicking more closely a physiological environment (37°C, submerged in PBS), the compressive strength of the non-sintered specimens after 1 hour decreased to 0.77 ± 0.15 MPa, 4.71 ± 1.01 MPa, 5.19 ± 0.78 MPa and 12.15 ± 2.08 MPa for the 0%, 5%, 10% and 15% silk materials, respectively. A longer immersion time was tested to investigate the effect of immersion duration on compressive strength. After 24 hours immersed in PBS, no further significant change in compressive strength was observed (Fig. S1). From the perspective of 3D printing, the silk-HAP paste could easily be extruded to deposit a steady filament that could be stacked for silk concentrations up to ~10% silk. Higher concentrations of silk resulted in extrusion issues during the printing process, and poor shape fidelity of the printed parts. Thus, the experiments described later in this study all used constructs printed with the 10% silk concentration.

2. Cytocompatibility of the 3D printed constructs

To assess the cytocompatibility of the 3D printed constructs, human mesenchymal stem cells (hMSCs) were seeded onto the constructs and allowed to adhere and proliferate. The cells attached rapidly on the surface of the filaments of the 3D printed scaffolds, and completely covered the scaffolds by 24h of culture. AlamarBlue metabolism was used to quantitatively assess cell survival on the constructs, along with tissue culture plastic controls; cell metabolism increased over 21 days, before reaching a plateau between days 21 and 35 (Fig 2.a). After 35 days of culture, the surfaces of the constructs were covered with hMSCs and the macropores and the space between the filaments in the scaffolds had started to fill with new matrix or tissue (Fig. 2.b, Fig. 2.c).

3. Osteoconductivity

The main application of 3D printing bone cements as a potential alternative for bone grafts in orthopedic surgery requires osteoconductivity of the constructs to sustain osteogenic differentiation. Human MSCs were seeded onto the constructs, allowed to adhere and spread, and then either left in traditional cell culture medium or switched to osteogenic

differentiation medium. After 21 days of culture, the activity of alkaline phosphatase (ALP), an indicator of bone metabolism [54], was assessed. To account for differences in cells in the growth medium vs. osteogenic medium, ALP activity was normalized to the amount of protein present. The hMSCs grown on the 3D printed constructs in the presence of osteogenic medium had normalized ALP activity increased from 4.91 ± 6.32 to 156.5 ± 84.97 after 21 days of culture (Fig. 3.a, top). This differentiation toward an osteoblastic lineage was further evidenced qualitatively by alkaline phosphatase staining, which showed ALP-positive cells covering the surface of the 3D printed constructs (Fig. 3.a, bottom). Due to the high calcium content in the silk/HAP bone cement, traditional histological staining for tissue mineralization (e.g., Von Kossa or Alizarin Red) could not be carried out, so late differentiation was assessed using confocal microscopy. After 35 days of culture, osteoblastic differentiation was assessed using immunofluorescent staining for Osteopontin (OPN) [55]. In the osteogenic medium and on the 3D printed constructs, the cells showed increased expression of OPN, demonstrating their osteoconductive properties (Fig. 3.b). Some OPN expression was observed in the growth medium, but much less marked than in the osteogenic medium.

4. Functionalization of the bone cement

Assessment of growth factor release—To analyze if the growth factors incorporated in the scaffolds either during (Printed) or after (Soaked) the 3D-printing process were released over time into the medium, an enzyme-linked immunosorbent assay (ELISA) was performed. Unloaded scaffolds (Control) and loaded with 1 μg of either BMP-2, VEGF or NGF, or the three factors together (BVN samples) were immersed PBS, incubated at 37°C and samples were taken after 1, 3, 6 and 12h, and 1, 3, 5 and 7d from five independent samples. For all the factors analyzed, the control samples showed no released. In the case of BMP-2, all samples including single and triple factor printed and soaked samples showed a similar pattern of release, with a peak between 6–12h incubation (Fig. 4.a). Interestingly, the release was low, reaching a maximum cumulative release after 7d of 2.5–3.5% of the total BMP-2 added (Fig. 4.b). In the case of VEGF, the soaked samples showed a maximum release after 1d incubation, while the VEGF printed as well as both BVN samples showed a maximum release after 5d incubation (Fig. 4.c). Importantly, the VEGF and BVN printed samples showed lower cumulative release reaching 5% and 25% release, respectively, after 7d incubation. The soaked samples showed a higher cumulative release with the BVN, with the highest release (70%), followed by the VEGF soaked samples (45%) (Fig. 4.d). Finally, in the case of NGF, all samples showed a maximum release between 12 and 24h of incubation (Fig. 4.e). Interestingly, again the printed samples showed a lower cumulative release with a maximum of about 20% after 7d, while the soaked samples showed a higher cumulative release. As in the case of VEGF the BVN soaked samples, the highest release after 7d averaged 60% followed by VEGF-soaked samples with an average of 50% release.

Osteoinduction—After noting the osteoconductivity of the 3D printed constructs, we incorporated BMP2 into the biomaterial and analyzed the osteoinductive effect of this osteogenic factor when this factor was added to the silk and printed as part of the scaffold. We also loaded BMP2 into the dried constructs after printing, to investigate potential differences that BMP2 presentation had on osteoblastic differentiation of hMSCs. BMP2

is an osteoinductive morphogen [56,57], and incorporating BMP2 into the bone cement did not impact the extrusion of the paste for the 3D printed constructs. hMSCs were seeded on these functionalized 3D printed constructs, kept in culture for 7 days. The cells were then lysed, RNA extracted, and the expression of genes associated to osteoblastic differentiation Runt-related Transcription Factor 2 (Runx2), Osteopontin (OPN) and Bone Sialoprotein (BSP) was assessed by qRTPCR and compared to control cells seeded on scaffolds growing in osteogenic medium and in the absence of extra growth factors.

The cells seeded on scaffolds including the BMP2 in the printing process ("printed") showed a 2, 2.5 and 10 log-fold increase in gene expression of Runx2 (Fig. 5.a), OPN (Fig. 5.b) and BSP (Fig. 5.c) respectively, in comparison to controls without BMP-2. Runx2 increase in expression was just a trend, while the upregulation of OPN and BSP was statistically significant. Notably, there was a positive trend but not statistically significant in the induction for the printed BMP-2 when compared to the samples containing BMP-2 loaded after the printing process.

Vascularization—The bone cement was functionalized with VEGF, and the migration and proliferation of human umbilical vein endothelial cells (HUVECs) was assessed. These cell responses were assessed at different time scales: 3 hours for migration, and up to 7 days for HUVEC proliferation. Migration was assessed using a transwell migration assay, commonly used to evaluate the response of endothelial cells to a chemotactic signal like VEGF [58]. Cells were allowed to migrate for three hours before being fixed and their nuclei stained with DAPI. To quantify migration, photomicrographs were taken in each well, and cell coverage was quantitatively assessed by measuring the coverage of the migrated cells on the bottom of the transwell. The data showed that the presence of VEGF supported a slight but not statistically significant increase in rate of cell migration when compared to the constructs without VEGF (7.7% vs. 5.9%, respectively; Fig. 5.d). When the VEGF was loaded into the 3D printed scaffolds by soaking the dried constructs in a VEGF solution, however, there was a statistically significant increase of migrated cells to 11.6%, suggesting that the VEGF loaded in these constructs was accessible and bioactive, inducing the cell responses in the migration assay (Fig. 5.d).

VEGF is known to have an effect on the proliferation of endothelial cells. AlamarBlue metabolism was used to quantitatively assess cell survival on the constructs 3 and 7 days after seeding (Fig. 5.e). The unloaded constructs showed no significant increase in cell metabolism between days 3 and 7; the constructs loaded with VEGF either printed or soaked showed a statistically significant increase in cell metabolism, indicating that the VEGF was still bioactive in both forms. Interestingly, at 7 days cells on the constructs printed with VEGF in the ink had a significantly higher cell metabolism that those on the constructs soaked in the VEGF, despite no significant difference measured at day 3.

Innervation—NGF was loaded into the bone cement prior to and after printing to assess the capability of the 3D printed constructs to induce nerve cell responses. The constructs were seeded with human induced neural stem cells (hiNSCs) and kept in culture for 7 days. There is evidence in the literature regarding the proliferative effect of NGF on neural stem cells, so cell viability after 7 days was assessed using alamarBlue. The hiNSCs adhered and

proliferated on the constructs compared to plastic controls, regardless of the presence or absence of the NGF. NGF loading did not affect cell proliferation, as there was a decrease in cell metabolism for the constructs soaked in NGF after printing compared to the unloaded constructs (Fig. 5.f).

To demonstrate that the NGF loaded into the silk-HAp scaffolds was still active and able to elicit a response by the cells, NSCs were seeded onto scaffolds soaked or printed with NGF and incubated for 3 days. Gene expression of Nestin, a marker for NSCs, and Tubulin β3 (Tubb3) and Microtubule Associated Protein 2 (MAP2), markers for differentiated neurons, was monitored via qPCR (Fig. 6). No statistical differences were found for the expression of Nestin when gene expression was compared to control samples (Fig. 6.a).

However, statistical differences were observed for Tubb3 and MAP2 markers for the soaked samples with a 6 and 8 fold increase, respectively (Fig 6.b,c). Interestingly, the printed samples showed no statistical differences when compared to the control samples (Fig. 6.b,c).

5. Effect of BMP2, VEGF and NGF on osteoblastic differentiation of hMSCs

To study the effect and potential synergy of different growth factors on osteoinduction in hMSCs, transcript expression of Runx2, OPN and BSP osteogenic markers of cells seeded on scaffolds soaked with growth factors, was monitored by qRTPCR. The osteogenic factor BMP-2, vascular VEGF or neural NGF growth factors, or the different mixtures of them, were incorporated into the scaffolds after the printing process (“soaked”). After 7d, cells seeded on BMP-2 and VEGF loaded scaffolds as well as BMP2 and NGF loaded scaffolds showed statistically significant increased induction of gene expression of Runx2 marker (Fig. 7.a), while all groups showed a trend of increased gene expression for all markers analyzed (Fig. 7.a–c) compared to control cells seeded on scaffolds growing in osteogenic medium and in the absence of exogenous growth factors. The highest level of induction for markers Runx2 and OP was observed for treatment group BMP2 and VEGF loaded scaffolds, whereas for BSP marker the highest induction observed corresponded to the combination of the three growth factors BMP2, VEGF and NGF treatment group (Fig. 5a–c).

Discussion

The development of injectable bone cements has filled a gap in treatment options for severe bone injuries that require surgical approaches and implanted materials. This alternative to autografts, allografts and xenografts can potentially overcome the limitations of available bone tissue, donor site morbidity, or disease transmission. In the context of 3D printing bone scaffolds, the extrusion of a bone cement to generate a patient-tailored and macroporous implant provides the possibility of developing patient-tailored solutions for large or pathological bone defects. These 3D printed bone cements must fulfill several requirements to provide optimal patient outcomes, including mechanical and biological performance, osseointegration and osteoinductivity. The importance of proper vascularization and innervation on bone outcomes is well documented in the literature [49,59–65], suggesting that incorporating the repair of the neurovascular network could be a promising tool for the accelerated regeneration of mature, high-quality bone tissue.

The mechanical properties of the materials reported here are close to those of trabecular bone, matching the properties of the surrounding tissue. Indeed, the ultimate compressive strength of trabecular bone in the human mandible ranges from 0.22 to 10.44 MPa, with a mean value of 3.9 MPa [66]. With a compressive strength of 5.19 ± 0.78 MPa, the 10% silk bone cement used in this study would therefore meet the requirements in terms of mechanics for the field of dental and craniofacial surgery. Implant mechanics are also important since the differentiation pathways of stem cells are also affected by substrate mechanics [67,68]. Overall, the properties of the 3D printed constructs suggest that this biomaterial would be suited for non-load bearing applications, for example alveolar ridge augmentation following bone resorption.

Osseointegration

The properties of the bone cement and the 3D printed constructs suggest osseointegration benefits. The macroporosity of the constructs can be optimized using 3D printing for bone growth and osseointegration [6]. The control over shape and geometry allows a match to the patient's anatomy, resulting in a closer fit and therefore improved osseointegration. This match should also yield better outcomes in terms of esthetics and mechanical transduction of forces from the surrounding bone tissue to the implanted material.

Cytocompatibility and osteoconductivity

The bone cement was cytocompatible; hMSCs adhered, survived, and proliferated on and in the constructs, colonizing the macropores between the filaments in all directions and also surviving throughout the depth of the constructs. Since MSCs are proangiogenic, the ability of the hMSCs to grow deep in the constructs is a promising indicator for vascularization of the 3D printed implants in large bone defects [69,70]. The constructs were osteoconductive, as evidenced by their ability to sustain the osteoblastic differentiation of hMSCs based on the upregulation of osteogenic genes like Runx2, OPN, or BSP. This was further confirmed by the increased activity of ALP and the immunofluorescent staining of OPN within 5 weeks in vitro.

Functionalization

Bone cements have been increasingly used as vectors for localized drug delivery, in particular for antimicrobial agents, but also for growth factors and morphogens, including osteogenic factors like BMP2 [71–73]. Functionalizing the material with bioactive molecules is crucial to induce more rapid bone growth, along with innervation and vascularization. We selected BMP2 for bone formation, VEGF for vascularization, and NGF for innervation, as these three factors are well-described in the literature with functional roles towards the tissue goals planned.

BMP2: The effects of the potent morphogen BMP2 on bone formation have been extensively documented in the literature [56,57]. Further, the localized presentation of osteogenic morphogens like BMP2 at the implantation site and the sustained presentation of lower concentrations of osteoinductive biomolecules can support the rapid formation of high-quality bone, reducing convalescence and side-effects like ectopic bone formation or pain [74]. Here, we showed that BMP2 could be loaded into the construct and

retain bioactivity, as evidenced by the osteogenic differentiation of hMSCs on BMP2-functionalized constructs. The potential of silk for drug delivery, both as a vehicle and due to its stabilizing effect on bioactive molecules and enzymes is well-documented in the literature [29,31,75–78]. The stabilizing effect of silk on complex proteins like BMP2 circumvents issues of loss of stability which frequently limit the use of morphogens [79]. Previous studies have shown that BMP2 can be loaded into silk-based materials, and be delivered in a sustained manner while maintaining its osteogenic properties [80–84].

VEGF: VEGF plays a major role in angiogenesis and the VEGF pathway is a key regulator of vascular regeneration which is critical for bone regeneration [62]. VEGF can be loaded into silk materials and be released in a sustained manner while maintaining its proangiogenic effect [83,85–88]. Besides its angiogenic properties, VEGF has also been shown to be osteogenic [59,63,64]; VEGF has a synergistic effect with osteoinductive factors like BMPs. For example, the delivery of VEGF-A with BMP2 (rat critical size defect model) enhanced BMP2-induced bone formation [65]. From an angiogenic perspective, there is an upregulation of VEGF and Vascular Endothelial Growth Factor – Receptor (VEGF-R) in the tips of invasive angiogenic sprouts, and blocking VEGF decreased microvessel outgrowth [89,90]. VEGF promoted von Willebrand factor release, integrin expression, interstitial collagenase expression, plasminogen activator and plasminogen activator receptor expression, and increased vascular permeability and fenestration [90]. There is also evidence that VEGF presented in an ECM-bound manner promotes endothelial cell adhesion, migration, and survival [91]. These studies suggested that a tissue engineering approach that mimics the physiological ECM-bound presentation of VEGF may lead to improved endothelial cell response, and therefore angiogenesis. This could explain the effect of the printed VEGF on HUVEC proliferation after 7 days. If the VEGF is sequestered in the construct and presented in an ECM-like manner to the cells, this may promote cell responses. A possible explanation for this is potential synergistic crosstalk between integrins and VEGF-receptors at the cell surface. However, this effect could also be explained by differences in release kinetics between the VEGF loaded before (printed) or after (soaked) in the 3D printed constructs. We posit that growth factors loaded in the constructs prior to printing will be released in a sustained manner, and therefore retain bioactivity for longer time frames. This hypothesis was supported by the transmigration assay, where early chemotactic migration of the HUVECs was increased by the VEGF loaded into the constructs post printing. These results suggest that the VEGF loaded in this manner was released rapidly from the construct, while VEGF loaded in the bone cement before printing was retained in the construct.

NGF: NGF signaling through the action of the neurotrophic tyrosine kinase receptor type 1 (TrkA) acts as a skeletal neurotrophin to promote the innervation of long bones, while coordinating vascularization and ossification [60]. This NGF-TrkA signaling in sensory nerves has been reported as necessary for fracture repair [49], as well as involved in skeletal adaptation to mechanical loads in mice [61], making it an important candidate for the bone/blood vessel/nerve model generated here. NGF can be loaded into silk biomaterials and be released in a sustained manner while maintaining bioactivity, and its presence increases neurite extension [92,93].

Additional rationale for choosing the specific growth factors comes from the synergistic effects and crosstalk between BMP2 and VEGF [65], VEGF and NGF [94], and NGF and BMP2 [95]. Some of these synergistic effects are evidenced in the upregulation of osteoblastic genes in the presence of these morphogens. As expected, BMP-2 induced increased expression of Runx2, OPN and BSP in hMSCs, and this effect was further increased in the presence of VEGF or NGF. The effect of the loading of all three factors needs to be elucidated, as there was an increased in BSP expression only for this condition. While this might reflect antagonistic crosstalk between VEGF and NGF, it could also be due to different rates of differentiation. Further investigation of the signaling pathways and of gene expression over time would be required to further understand the underlying mechanisms for further optimization of outcomes.

The loading conditions and resulting release kinetics are relevant, as all three morphogens have enhanced bioactivity when released slowly over weeks [96–98]. This sustained activity likely contributes to faster repair of mature, high-quality bone tissue, and the functional regeneration of neurovascular networks. The use of 3D printing for these scaffolds offers not only the control of geometry, architecture, and porosity, but it also allows for the modulation of surface-to-volume ratio by modulating filament diameter. This control can be used to tune the diffusion of bioactive molecules from the construct, as well as mechanics and in vivo degradation rate. Printing morphogens and cytokines directly in the bone cement provides prospects for in vivo utility, using spatially controlled deposition of bioactive molecules to guide regeneration.

Further studies would benefit from exploring the signaling pathways and crosstalk between multiple cell types grown in coculture systems to optimize the outcomes identified in the present work. Due to the multiple growth factors/morphogens and different cell types, multiple synergistic or antagonistic effects are involved, thus, we anticipate ectopic and orthotopic bone models would be most useful to help elucidate these interactions as a next step.

Conclusions

The bone cement developed in this study displayed mechanical properties, cytocompatibility, and osteoconductivity, suggesting a promising material for bone defect repairs and for use in 3D printing approaches for this need. The control of geometry and macroporosity, and the ability to load with osteoinductive, angiogenic, and neurotrophic morphogens suggests that this approach has promise in terms of osseointegration when the systems are used in vivo. The current mechanics of the 3D prints are suitable for non-load bearing systems like dental, oral and maxillofacial surgery, and in particular alveolar ridge augmentation. Esthetics and osseointegration are attainable due to the ability to print with a resolution at the centimeter scale with control of filament deposition.

Supplementary Material

Refer to Web version on PubMed Central for supplementary material.

Acknowledgements

We thank the NIH (P41EB027062 and R01AR068048) for support of this work.

References

[1]. Roddy E, DeBaun MR, Daoud-Gray A, Yang YP, Gardner MJ, Treatment of critical-sized bone defects: clinical and tissue engineering perspectives, Eur. J. Orthop. Surg. Traumatol28 (2018) 351–362. 10.1007/s00590-017-2063-0. [PubMed: 29080923]

[2]. Campana V, Milano G, Pagano E, Barba M, Cicione C, Salonna G, Lattanzi W, Logroscino G, Bone substitutes in orthopaedic surgery: from basic science to clinical practice, J. Mater. Sci. Mater. Med25 (2014) 2445–2461. 10.1007/s10856-014-5240-2. [PubMed: 24865980]

[3]. Oryan A, Alidadi S, Moshiri A, Maffulli N, Bone regenerative medicine: Classic options, novel strategies, and future directions, J. Orthop. Surg. Res9 (2014) 1–27. 10.1186/1749-799X-9-18. [PubMed: 24383821]

[4]. Amini AR, Laurencin CT, Nukavarapu SP, Bone tissue engineering: Recent advances and challenges, Crit. Rev. Biomed. Eng40 (2012) 363–408. 10.1615/CritRevBiomedEng.v40.i5.10. [PubMed: 23339648]

[5]. Jayesh RS, Dhinakarsamy V, Osseointegration, J. Pharm. Bioallied Sci7 (2015) S226–S229. 10.4103/0975-7406.155917. [PubMed: 26015719]

[6]. Karageorgiou V, Kaplan D, Porosity of 3D biomaterial scaffolds and osteogenesis, Biomaterials26 (2005) 5474–5491. 10.1016/j.biomaterials.2005.02.002. [PubMed: 15860204]

[7]. Gao X, Fraulob M, Haïat G, Biomechanical behaviours of the bone-implant interface: A review, J. R. Soc. Interface16 (2019). 10.1098/rsif.2019.0259.

[8]. Albrektsson T, Johansson C, Osteoinduction, osteoconduction and osseointegration, Eur. Spine J10 (2001) S96–S101. 10.1007/s005860100282. [PubMed: 11716023]

[9]. Fernandez de Grado G, Keller L, Idoux-Gillet Y, Wagner Q, Musset AM, Benkirane-Jessel N, Bornert F, Offner D, Bone substitutes: a review of their characteristics, clinical use, and perspectives for large bone defects management, J. Tissue Eng9 (2018). 10.1177/2041731418776819.

[10]. Roberts TT, Rosenbaum AJ, Bone grafts, bone substitutes and orthobiologics the bridge between basic science and clinical advancements in fracture healing, Organogenesis8 (2012) 114–124. 10.4161/org.23306. [PubMed: 23247591]

[11]. Dall'Oca C, Maluta T, Cavani F, Morbioli GP, Bernardi P, Sbarbati A, Degl'Innocenti D, Magnan B, The biocompatibility of porous vs non-porous bone cements: new methodological approach, Eur. J. Histochem58 (2014) 95–102. 10.4081/ejh.2014.2255.

[12]. Zhang M, Lin R, Wang X, Xue J, Deng C, Feng C, Zhuang H, Ma J, Qin C, Wan L, Chang J, Wu C, 3D printing of Haversian bone-mimicking scaffolds for multicellular delivery in bone regeneration, Sci. Adv6 (2020). 10.1126/sciadv.aaz6725.

[13]. El-Rashidy AA, Roether JA, Harhaus L, Kneser U, Boccaccini AR, Regenerating bone with bioactive glass scaffolds: A review of in vivo studies in bone defect models, Acta Biomater62 (2017) 1–28. 10.1016/j.actbio.2017.08.030. [PubMed: 28844964]

[14]. Kim HJ, Kim UJ, Kim HS, Li C, Wada M, Leisk GG, Kaplan DL, Bone tissue engineering with premineralized silk scaffolds, Bone42 (2008) 1226–1234. 10.1016/j.bone.2008.02.007. [PubMed: 18387349]

[15]. Correia C, Bhumiratana S, Yan LP, Oliveira AL, Gimble JM, Rockwood D, Kaplan DL, Sousa RA, Reis RL, Vunjak-Novakovic G, Development of silk-based scaffolds for tissue engineering of bone from human adipose-derived stem cells, Acta Biomater8 (2012) 2483–2492. 10.1016/j.actbio.2012.03.019. [PubMed: 22421311]

[16]. Mandal BB, Grinberg A, Gil ES, Panilaitis B, Kaplan DL, High-strength silk protein scaffolds for bone repair, Proc. Natl. Acad. Sci. U. S. A109 (2012) 7699–7704. 10.1073/pnas.1119474109. [PubMed: 22552231]

[17]. Wu J, Cao L, Liu Y, Zheng A, Jiao D, Zeng D, Wang X, Kaplan DL, Jiang X, Functionalization of Silk Fibroin Electrospun Scaffolds via BMSC Affinity Peptide Grafting through Oxidative

Self-Polymerization of Dopamine for Bone Regeneration, ACS Appl. Mater. Interfaces11 (2019) 8878–8895. 10.1021/acsami.8b22123. [PubMed: 30777748]

[18]. Hofmann S, Hilbe M, Fajardo RJ, Hagenmüller H, Nuss K, Arras M, Müller R, Von Rechenberg B, Kaplan DL, Merkle HP, Meinel L, Remodeling of tissue-engineered bone structures in vivo, Eur. J. Pharm. Biopharm85 (2013) 119–129. 10.1016/j.ejpb.2013.02.011. [PubMed: 23958323]

[19]. Gomes S, Gallego-Llamas J, Leonor IB, Mano JF, Reis RL, Kaplan DL, In Vivo Biological Responses to Silk Proteins Functionalized with Bone Sialoprotein, Macromol. Biosci13 (2013) 444–454. 10.1002/mabi.201200372. [PubMed: 23359587]

[20]. Wray LS, Rnjak-Kovacina J, Mandal BB, Schmidt DF, Gil ES, Kaplan DL, A silk-based scaffold platform with tunable architecture for engineering critically-sized tissue constructs, Biomaterials33 (2012) 9214–9224. 10.1016/j.biomaterials.2012.09.017. [PubMed: 23036961]

[21]. Zhang W, Zhu C, Wu Y, Ye D, Wang S, Zou D, Zhang X, Kaplan DL, Jiang X, VEGF and BMP-2 promote bone regeneration by facilitating bone marrow stem cell homing and differentiation, Eur. Cells Mater27 (2014) 1–12. 10.22203/eCM.v027a01.

[22]. Perrone GS, Leisk GG, Lo TJ, Moreau JE, Haas DS, Papenburg BJ, Golden EB, Partlow BP, Fox SE, Ibrahim AMS, Lin SJ, Kaplan DL, The use of silk-based devices for fracture fixation, Nat. Commun5 (2014) 1–9. 10.1038/ncomms4385.

[23]. Meinel L, Betz O, Fajardo R, Hofmann S, Nazarian A, Cory E, Hilbe M, McCool J, Langer R, Vunjak-Novakovic G, Merkle HP, Rechenberg B, Kaplan DL, KirkerHead C, Silk based biomaterials to heal critical sized femur defects, Bone39 (2006) 922–931. 10.1016/j.bone.2006.04.019. [PubMed: 16757219]

[24]. Zhang W, Zhu C, Ye D, Xu L, Zhang X, Wu Q, Zhang X, Kaplan DL, Jiang X, Porous silk scaffolds for delivery of growth factors and stem cells to enhance bone regeneration, PLoS One9 (2014) 1–9. 10.1371/journal.pone.0102371.

[25]. Ding X, Yang G, Zhang W, Li G, Lin S, Kaplan DL, Jiang X, Increased stem cells delivered using a silk gel/scaffold complex for enhanced bone regeneration, Sci. Rep7 (2017) 1–10. 10.1038/s41598-017-02053-z. [PubMed: 28127051]

[26]. Roohaniesfahani I, Wang J, No YJ, de Candia C, Miao X, Lu Z, Shi J, Kaplan DL, Jiang X, Zreiqat H, Modulatory effect of simultaneously released magnesium, strontium, and silicon ions on injectable silk hydrogels for bone regeneration, Mater. Sci. Eng. C94 (2019) 976–987. 10.1016/j.msec.2018.10.053.

[27]. Zhang L, Liu X, Li G, Wang P, Yang Y, Tailoring degradation rates of silk fibroin scaffolds for tissue engineering, J. Biomed. Mater. Res. - Part A107 (2019) 104–113. 10.1002/jbm.a.36537.

[28]. Wang Z, Wang Z, Lu WW, Zhen W, Yang D, Peng S, Novel biomaterial strategies for controlled growth factor delivery for biomedical applications, NPG Asia Mater9 (2017) e435–17. 10.1038/am.2017.171.

[29]. Pritchard EM, Dennis PB, Omenetto F, Naik RR, Kaplan DL, Review: Physical and chemical aspects of stabilization of compounds in silk, Biopolymers97 (2012) 479–498. 10.1002/bip.22026. [PubMed: 22270942]

[30]. Tao H, Marelli B, Yang M, An B, Onses MS, Rogers JA, Kaplan DL, Omenetto FG, Inkjet Printing of Regenerated Silk Fibroin: From Printable Forms to Printable Functions, Adv. Mater27 (2015) 4273–4279. 10.1002/adma.201501425. [PubMed: 26079217]

[31]. Li AB, Kluge JA, Guziewicz NA, Omenetto FG, Kaplan DL, Silk-based stabilization of biomacromolecules, J. Control. Release219 (2015) 416–430. 10.1016/j.jconrel.2015.09.037. [PubMed: 26403801]

[32]. Ding Z, Han H, Fan Z, Lu H, Sang Y, Yao Y, Cheng Q, Lu Q, Kaplan DL, Nanoscale Silk-Hydroxyapatite Hydrogels for Injectable Bone Biomaterials, ACS Appl. Mater. Interfaces9 (2017) 16913–16921. 10.1021/acsami.7b03932. [PubMed: 28471165]

[33]. Swetha M, Sahithi K, Moorthi A, Srinivasan N, Ramasamy K, Selvamurugan N, Biocomposites containing natural polymers and hydroxyapatite for bone tissue engineering, Int. J. Biol. Macromol47 (2010) 1–4. 10.1016/j.ijbiomac.2010.03.015. [PubMed: 20361991]

[34]. Lee CM, Yang SW, Jung SC, Kim BH, Oxygen plasma treatment on 3D-printed chitosan/gelatin/hydroxyapatite scaffolds for bone tissue engineering, J. Nanosci. Nanotechnol17 (2017) 2747–2750. 10.1166/jnn.2017.13337. [PubMed: 29664596]

[35]. Kuroiwa Y, Niikura T, Lee SY, Oe K, Iwakura T, Fukui T, Matsumoto T, Matsushita T, Nishida K, Kuroda R, Escherichia coli-derived BMP-2-absorbed β-TCP granules induce bone regeneration in rabbit critical-sized femoral segmental defects, Int. Orthop43 (2019) 1247–1253. 10.1007/s00264-018-4079-4. [PubMed: 30097727]

[36]. Boda SK, Almoshari Y, Wang H, Wang X, Reinhardt RA, Duan B, Wang D, Xie J, Mineralized nanofiber segments coupled with calcium-binding BMP-2 peptides for alveolar bone regeneration, Acta Biomater85 (2019) 282–293. 10.1016/j.actbio.2018.12.051. [PubMed: 30605770]

[37]. Abdel-Salam FS, Elkheshen SA, Mahmoud AA, Basalious EB, Amer MS, Mostafa AA, Elkasabgy NA, In-situ forming chitosan implant-loaded with raloxifene hydrochloride and bioactive glass nanoparticles for treatment of bone injuries: Formulation and biological evaluation in animal model, Int. J. Pharm580 (2020). 10.1016/j.ijpharm.2020.119213.

[38]. Quade M, Vater C, Schlootz S, Bolte J, Langanke R, Bretschneider H, Gelinsky M, Goodman SB, Zwingenberger S, Strontium enhances BMP-2 mediated bone regeneration in a femoral murine bone defect model, J. Biomed. Mater. Res. - Part B Appl. Biomater108 (2020) 174–182. 10.1002/jbm.b.34376.

[39]. Jabbarzadeh E, Blanchette J, Shazly T, Khademhosseini A, Camci-Unal G, Laurencin C, Vascularization of Biomaterials for Bone Tissue Engineering: Current Approaches and Major Challenges, Curr. Angiogenesise1 (2012) 180–191. 10.2174/2211552811201030180.

[40]. Will J, Melcher R, Treul C, Travitzky N, Kneser U, Polykandriotis E, Horch R, Greil P, Porous ceramic bone scaffolds for vascularized bone tissue regeneration, J. Mater. Sci. Mater. Med19 (2008) 2781–2790. 10.1007/s10856-007-3346-5. [PubMed: 18305907]

[41]. Nguyen LH, Annabi N, Nikkhah M, Bae H, Binan L, Park S, Kang Y, Yang Y, Khademhosseini A, Vascularized bone tissue engineering: Approaches for potential improvement, Tissue Eng. - Part B Rev18 (2012) 363–382. 10.1089/ten.teb.2012.0012. [PubMed: 22765012]

[42]. Yan Y, Chen H, Zhang H, Guo C, Yang K, Chen K, Cheng R, Qian N, Sandler N, Zhang YS, Shen H, Qi J, Cui W, Deng L, Vascularized 3D printed scaffolds for promoting bone regeneration, Biomaterials190–191 (2019) 97–110. 10.1016/j.biomaterials.2018.10.033.

[43]. Liu X, Jakus AE, Kural M, Qian H, Engler A, Ghaedi M, Shah R, Steinbacher DM, Niklason LE, Vascularization of Natural and Synthetic Bone Scaffolds, Cell Transplant27 (2018) 1269–1280. 10.1177/0963689718782452. [PubMed: 30008231]

[44]. Yin S, Zhang W, Zhang Z, Jiang X, Recent Advances in Scaffold Design and Material for Vascularized Tissue-Engineered Bone Regeneration, Adv. Healthc. Mater8 (2019) 1–19. 10.1002/adhm.201801433.

[45]. Chenu C, Role of innervation in the control of bone remodeling, J. Musculoskelet. Neuronal Interact4 (2004) 132–134. [PubMed: 15615111]

[46]. Milovanović P, Đurić M, Innervation of bones: Why it should not be neglected?, Med. Podml69 (2018) 25–32. 10.5937/mp69-18404.

[47]. Gkiatas I, Papadopoulos D, Pakos EE, Kostas-Agnantis I, Gelalis I, Vekris M, Korompilias A, The multifactorial role of peripheral nervous system in bone growth, Front. Phys5 (2017) 1–6. 10.3389/fphy.2017.00044.

[48]. Sayilekshmy M, Hansen RB, Delaissé JM, Rolighed L, Andersen TL, Heegaard AM, Innervation is higher above Bone Remodeling Surfaces and in Cortical Pores in Human Bone: Lessons from patients with primary hyperparathyroidism, Sci. Rep9 (2019) 1–14. 10.1038/s41598-019-41779-w. [PubMed: 30626917]

[49]. Li Z, Meyers CA, Chang L, Lee S, Li Z, Tomlinson R, Hoke A, Clemens TL, James AW, Fracture repair requires TrkA signaling by skeletal sensory nerves, J. Clin. Invest129 (2019) 5137–5150. 10.1172/JCI128428. [PubMed: 31638597]

[50]. Rockwood DN, Preda RC, Yücel T, Wang X, Lovett ML, Kaplan DL, Materials fabrication from Bombyx mori silk fibroin, Nat. Protoc6 (2011) 1612–1631. 10.1038/nprot.2011.379. [PubMed: 21959241]

[51]. Cairns DM, Chwalek K, Moore YE, Kelley MR, Abbott RD, Moss S, Kaplan DL, Expandable and Rapidly Differentiating Human Induced Neural Stem Cell Lines for Multiple Tissue

Engineering Applications, Stem Cell Reports7 (2016) 557–570. 10.1016/j.stemcr.2016.07.017. [PubMed: 27569063]

[52]. Livak KJ, Schmittgen TD, Analysis of relative gene expression data using real-time quantitative PCR and the 2-ΔΔCT method, Methods25 (2001) 402–408. 10.1006/meth.2001.1262. [PubMed: 11846609]

[53]. Hu X, Shmelev K, Sun L, Gil ES, Park SH, Cebe P, Kaplan DL, Regulation of silk material structure by temperature-controlled water vapor annealing, Biomacromolecules12 (2011) 1686–1696. 10.1021/bm200062a. [PubMed: 21425769]

[54]. Castrén E, Sillat T, Oja S, Noro A, Laitinen A, Konttinen YT, Lehenkari P, Hukkanen M, Korhonen M, Osteogenic differentiation of mesenchymal stromal cells in two-dimensional and three-dimensional cultures without animal serum, Stem Cell Res. Ther6 (2015) 1–13. 10.1186/s13287-015-0162-6. [PubMed: 25559585]

[55]. Zohar R, Cheifetz S, McCulloch CAG, Sodek J, Analysis of intracellular osteopontin as a marker of osteoblastic cell differentiation and mesenchymal cell migration, Eur. J. Oral Sci106 (1998) 401–407. 10.1111/j.1600-0722.1998.tb02206.x. [PubMed: 9541256]

[56]. Wang RN, Green J, Wang Z, Deng Y, Qiao M, Peabody M, Zhang Q, Ye J, Yan Z, Denduluri S, Idowu O, Li M, Shen C, Hu A, Haydon RC, Kang R, Mok J, Lee MJ, Luu HL, Shi LL, Bone Morphogenetic Protein (BMP) signaling in development and human diseases, Genes Dis1 (2014) 87–105. 10.1016/j.gendis.2014.07.005. [PubMed: 25401122]

[57]. Sheikh Z, Javaid MA, Hamdan N, Hashmi R, Bone regeneration using bone morphogenetic proteins and various biomaterial carriers, Materials (Basel)8 (2015) 1778–1816. 10.3390/ma8041778. [PubMed: 28788032]

[58]. Pellet-Many C, Chemotactic migration of endothelial cells towards VEGF-A165, Methods Mol. Biol1332 (2015) 151–157. 10.1007/978-1-4939-2917-7_11. [PubMed: 26285752]

[59]. Street J, Bao M, DeGuzman L, Bunting S, Peale FV, Ferrara N, Steinmetz H, Hoeffel J, Cleland JL, Daugherty A, Van Bruggen N, Redmond HP, Carano RAD, Filvaroff EH, Vascular endothelial growth factor stimulates bone repair by promoting angiogenesis and bone turnover, Proc. Natl. Acad. Sci. U. S. A99 (2002) 9656–9661. 10.1073/pnas.152324099. [PubMed: 12118119]

[60]. Tomlinson RE, Li Z, Zhang Q, Goh BC, Li Z, Thorek DLJ, Rajbhandari L, Brushart TM, Minichiello L, Zhou F, Venkatesan A, Clemens TL, NGF-TrkA Signaling by Sensory Nerves Coordinates the Vascularization and Ossification of Developing Endochondral Bone, Cell Rep16 (2016) 2723–2735. 10.1016/j.celrep.2016.08.002. [PubMed: 27568565]

[61]. Tomlinson RE, Li Z, Li Z, Minichiello L, Riddle RC, Venkatesan A, Clemens TL, NGF-TrkA signaling in sensory nerves is required for skeletal adaptation to mechanical loads in mice, Proc. Natl. Acad. Sci. U. S. A114 (2017) E3632–E3641. 10.1073/pnas.1701054114. [PubMed: 28416686]

[62]. Keramaris NC, Calori GM, Nikolaou VS, Schemitsch EH, Giannoudis PV, Fracture vascularity and bone healing: A systematic review of the role of VEGF, Injury39 (2008). 10.1016/S0020-1383(08)70015-9.

[63]. Orlandini M, Spreafico A, Bardelli M, Rocchigiani M, Salameh A, Nucciotti S, Capperucci C, Frediani B, Oliviero S, Vascular endothelial growth factor-D activates VEGFR-3 expressed in osteoblasts inducing their differentiation, J. Biol. Chem281 (2006) 17961–17967. 10.1074/jbc.M600413200. [PubMed: 16624815]

[64]. Mayr-wohlfart U, Waltenberger J, Hausser H, Kessler S, Günther KP, Dehio C, Puhl W, Brenner RE, Vascular endothelial growth factor stimulates chemotactic migration of primary human osteoblasts, Bone30 (2002) 472–477. 10.1016/S8756-3282(01)00690-1. [PubMed: 11882460]

[65]. Patel ZS, Young S, Tabata Y, Jansen JA, Wong MEK, Mikos AG, Dual delivery of an angiogenic and an osteogenic growth factor for bone regeneration in a critical size defect model, Bone43 (2008) 931–940. 10.1016/j.bone.2008.06.019. [PubMed: 18675385]

[66]. Misch CE, Qu Z, Bidez MW, Mechanical properties of trabecular bone in the human mandible: Implications for dental implant treatment planning and surgical placement, J. Oral Maxillofac. Surg57 (1999) 700–706. 10.1016/S0278-2391(99)90437-8. [PubMed: 10368096]

[67]. Ivanovska IL, Shin JW, Swift J, Discher DE, Stem cell mechanobiology: Diverse lessons from bone marrow, Trends Cell Biol25 (2015) 523–532. 10.1016/j.tcb.2015.04.003. [PubMed: 26045259]

[68]. Engler AJ, Sen S, Sweeney HL, Discher DE, Matrix Elasticity Directs Stem Cell Lineage Specification, Cell126 (2006) 677–689. 10.1016/j.cell.2006.06.044. [PubMed: 16923388]

[69]. Tao H, Han Z, Han ZC, Li Z, Proangiogenic Features of Mesenchymal Stem Cells and Their Therapeutic Applications, Stem Cells Int2016 (2016). 10.1155/2016/1314709.

[70]. Vidal L, Kampleitner C, Brennan M, Hoornaert A, Layrolle P, Reconstruction of Large Skeletal Defects: Current Clinical Therapeutic Strategies and Future Directions Using 3D Printing, Front. Bioeng. Biotechnol (2020). 10.3389/fbioe.2020.00061.

[71]. Oortgiesen DA, Walboomers XF, Bronckers AL, Meijer GJ, Jansen JA, Periodontal regeneration using an injectable bone cement combined with BMP-2 or FGF-2, J. Tissue Eng. Regen. Med8 (2014) 202–209. 10.1002/term.1514. [PubMed: 22552898]

[72]. Wang B, Mastrogiacomo S, Yang F, Shao J, Ong MMA, Chanchareonsook N, Jansen JA, Walboomers XF, Yu N, Application of BMP-Bone Cement and FGF-Gel on Periodontal Tissue Regeneration in Nonhuman Primates, Tissue Eng. - Part C Methods. 25 (2019) 748–756. 10.1089/ten.tec.2019.0160. [PubMed: 31701811]

[73]. Gunnella F, Kunisch E, Bungartz M, Maenz S, Horbert V, Xin L, Mika J, Borowski J, Bischoff S, Schubert H, Hortschansky P, Sachse A, Illerhaus B, Günster J, Bossert J, Jandt KD, Plöger F, Kinne RW, Brinkmann O, Low-dose BMP-2 is sufficient to enhance the bone formation induced by an injectable, PLGA fiber-reinforced, brushite-forming cement in a sheep defect model of lumbar osteopenia, Spine J17 (2017) 1699–1711. 10.1016/j.spinee.2017.06.005. [PubMed: 28619686]

[74]. James AW, LaChaud G, Shen J, Asatrian G, Nguyen V, Zhang X, Ting K, Soo C, A Review of the Clinical Side Effects of Bone Morphogenetic Protein-2, Tissue Eng. - Part Rev22 (2016) 284–297. 10.1089/ten.teb.2015.0357.

[75]. Li AB, Kluge JA, Zhi M, Cicerone MT, Omenetto FG, Kaplan DL, Enhanced Stabilization in Dried Silk Fibroin Matrices, Biomacromolecules18 (2017) 2900–2905. 10.1021/acs.biomac.7b00857. [PubMed: 28777562]

[76]. Wenk E, Merkle HP, Meinel L, Silk fibroin as a vehicle for drug delivery applications, J. Control. Release150 (2011) 128–141. 10.1016/j.jconrel.2010.11.007. [PubMed: 21059377]

[77]. Pritchard EM, Szybala C, Boison D, Kaplan DL, Silk fibroin encapsulated powder reservoirs for sustained release of adenosine, J. Control. Release144 (2010) 159–167. 10.1016/j.jconrel.2010.01.035. [PubMed: 20138938]

[78]. Lu Q, Wang X, Hu X, Cebe P, Omenetto F, Kaplan DL, Stabilization and release of enzymes from silk films, Macromol. Biosci10 (2010) 359–368. 10.1002/mabi.200900388. [PubMed: 20217856]

[79]. El Bialy I, Jiskoot W, Reza Nejadnik M, Formulation, Delivery and Stability of Bone Morphogenetic Proteins for Effective Bone Regeneration, Pharm. Res34 (2017) 1152–1170. 10.1007/s11095-017-2147-x. [PubMed: 28342056]

[80]. Li C, Vepari C, Jin HJ, Kim HJ, Kaplan DL, Electrospun silk-BMP-2 scaffolds for bone tissue engineering, Biomaterials (2006). 10.1016/j.biomaterials.2006.01.022.

[81]. Karageorgiou V, Tomkins M, Fajardo R, Meinel L, Snyder B, Wade K, Chen J, Vunjak-Novakovic G, Kaplan DL, Porous silk fibroin 3-D scaffolds for delivery of bone morphogenetic protein-2 in vitro and in vivo, J. Biomed. Mater. Res. - Part A (2006). 10.1002/jbm.a.30728.

[82]. Sun J, Zhang Y, Li B, Gu Y, Chen L, Controlled release of BMP-2 from a collagenmimetic peptide-modified silk fibroin-nanohydroxyapatite scaffold for bone regeneration, J. Mater. Chem. B (2017). 10.1039/c7tb02043k.

[83]. Wang Q, Zhang Y, Li B, Chen L, Controlled dual delivery of low doses of BMP-2 and VEGF in a silk fibroin-nanohydroxyapatite scaffold for vascularized bone regeneration, J. Mater. Chem. B (2017). 10.1039/c7tb00949f.

[84]. Yan S, Feng L, Zhu Q, Yang W, Lan Y, Li D, Liu Y, Xue W, Guo R, Wu G, Controlled Release of BMP-2 from a Heparin-Conjugated Strontium-Substituted Nanohydroxyapatite/

Silk Fibroin Scaffold for Bone Regeneration, ACS Biomater. Sci. Eng (2018). 10.1021/acsbiomaterials.8b00459.

[85]. Zhang D, Cao N, Zhou S, Chen Z, Zhang X, Zhu W, The enhanced angiogenesis effect of VEGF-silk fibroin nanospheres-BAMG scaffold composited with adipose derived stem cells in a rabbit model, RSC Adv (2018). 10.1039/c7ra11610a.

[86]. Seib FP, Herklotz M, Burke KA, Maitz MF, Werner C, Kaplan DL, Multifunctional silk-heparin biomaterials for vascular tissue engineering applications, Biomaterials (2014). 10.1016/j.biomaterials.2013.09.053.

[87]. Wang B, Lv X, Chen S, Li Z, Yao J, Peng X, Feng C, Xu Y, Wang H, Bacterial cellulose/gelatin scaffold loaded with VEGF-silk fibroin nanoparticles for improving angiogenesis in tissue regeneration, Cellulose (2017). 10.1007/s10570-017-1472-x.

[88]. Zhang W, Wang X, Wang S, Zhao J, Xu L, Zhu C, Zeng D, Chen J, Zhang Z, Kaplan DL, Jiang X, The use of injectable sonication-induced silk hydrogel for VEGF 165 and BMP-2 delivery for elevation of the maxillary sinus floor, Biomaterials (2011). 10.1016/j.biomaterials.2011.08.047.

[89]. Gerhardt H, Golding M, Fruttiger M, Ruhrberg C, Lundkvist A, Abramsson A, Jeltsch M, Mitchell C, Alitalo K, Shima D, Betsholtz C, VEGF guides angiogenic sprouting utilizing endothelial tip cell filopodia, J. Cell Biol161 (2003) 1163–1177. 10.1083/jcb.200302047. [PubMed: 12810700]

[90]. Ucuzian AA, Gassman AA, East AT, Greisler HP, Molecular mediators of angiogenesis, J. Burn Care Res31 (2010) 158–175. 10.1097/BCR.0b013e3181c7ed82. [PubMed: 20061852]

[91]. Hutchings H, Ortega N, Plouët J, Extracellular matrix-bound vascular endothelial growth factor promotes endothelial cell adhesion, migration, and survival through integrin ligation., FASEB J17 (2003) 1520–1522. 10.1096/fj.02-0691fje. [PubMed: 12709411]

[92]. Dinis TM, Vidal G, Jose RR, Vigneron P, Bresson D, Fitzpatrick V, Marin F, Kaplan DL, Egles C, Complementary effects of two growth factors in multifunctionalized silk nanofibers for nerve reconstruction, PLoS One9 (2014) e109770. 10.1371/journal.pone.0109770. [PubMed: 25313579]

[93]. Uebersax L, Mattotti M, Papaloïzos M, Merkle HP, Gander B, Meinel L, Silk fibroin matrices for the controlled release of nerve growth factor (NGF), Biomaterials28 (2007) 4449–4460. 10.1016/j.biomaterials.2007.06.034. [PubMed: 17643485]

[94]. Lazarovici P, Marcinkiewicz C, Lelkes P, Cross Talk between the Cardiovascular and Nervous Systems:Neurotrophic Effects of Vascular Endothelial Growth Factor (VEGF) and Angiogenic Effects of Nerve Growth Factor (NGF)-Implications in Drug Development, Curr. Pharm. Des12 (2006) 2609–2622. 10.2174/138161206777698738. [PubMed: 16842161]

[95]. Lattanzi W, Parolisi R, Barba M, Bonfanti L, Osteogenic and neurogenic stem cells in their own place: Unraveling differences and similarities between niches, Front. Cell. Neurosci9 (2015). 10.3389/fncel.2015.00455.

[96]. Srouji S, Ben-David D, Lotan R, Livne E, Avrahami R, Zussman E, Slow-release human recombinant bone morphogenetic protein-2 embedded within electrospun scaffolds for regeneration of bone defect: In vitro and in vivo evaluation, Tissue Eng. - Part A17 (2011) 269–277. 10.1089/ten.tea.2010.0250. [PubMed: 20799887]

[97]. Zhu S, Segura T, Cell-Demanded VEGF Release via Nanocapsules Elicits Different Receptor Activation Dynamics and Enhanced Angiogenesis, Ann. Biomed. Eng44 (2016) 1983–1992. 10.1007/s10439-016-1581-y. [PubMed: 26940611]

[98]. Wang Z, Han N, Wang J, Zheng H, Peng J, Kou Y, Xu C, An S, Yin X, Zhang P, Jiang B, Improved peripheral nerve regeneration with sustained release nerve growth factor microspheres in small gap tubulization., Am. J. Transl. Res6 (2014) 413–21. [PubMed: 25075258]

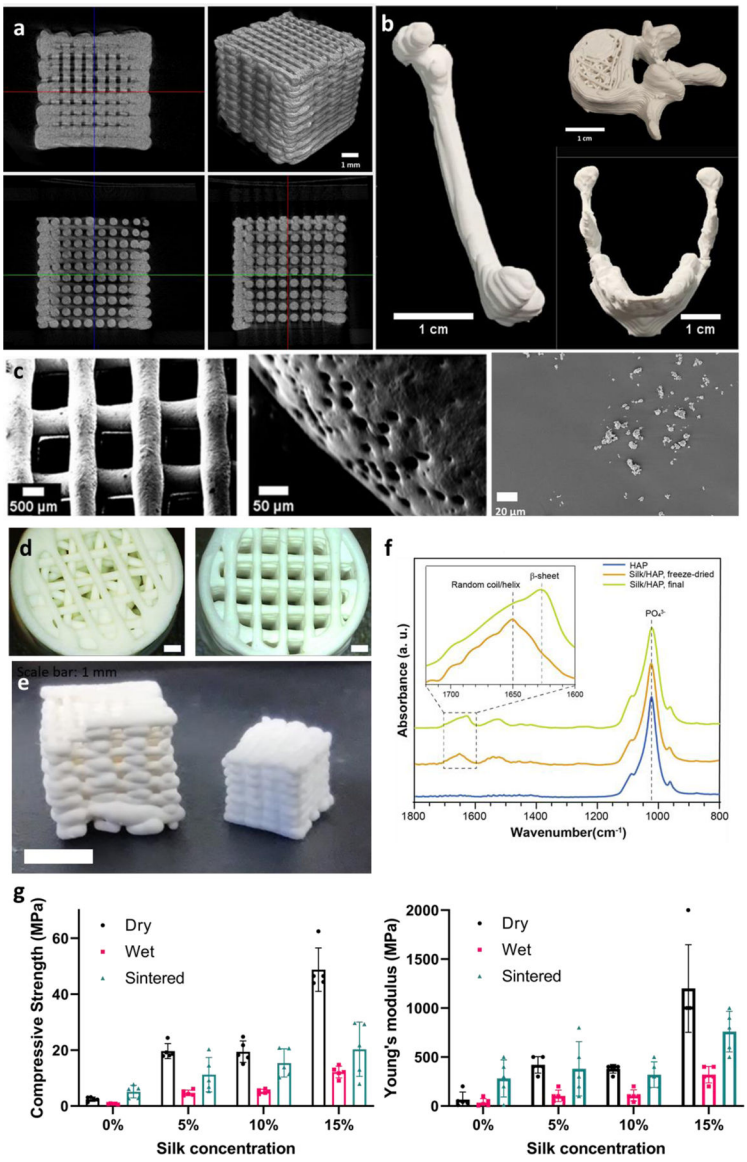

Figure 1:

Characterization of the silk-HAP material. (a) Microcomputed tomography of a 3D printed 10x10x10 mm cube, showing the general aspect of the cube (top right), regular filament distribution and interconnected pores. Scale bar: 1 mm. (b) 3D-printed anatomical structures: femur (left); vertebra (right, top); mandible (right, bottom). Scale bar: 1 cm. (c) Scanning electron micrograph (SEM) of a 3D-printed construct (left), showing control of filament deposition and macroporosity; of the surface of the filament, showing microporosity (center); of the hydroxyapatite (HAP) powder used for the silk-HAP bone cement, showing particle distribution (right). (d) 3D printed cylinders, showing microporosity and control of filament deposition. Scale bar: 1 mm. (e) Unsintered (left) and sintered (right) 10x10x10 mm cube, 3D printed using the 10% silk condition, showing the effect of sintering on aspect and size of the constructs. Scale bar: 5 mm. (f) FTIR spectra of the HAP powder, silk/HAP immediately after printing (freeze-dried), and of silk/HAP

after drying. (g) Compressive strength (MPa) and Young's modulus of silk/hydroxyapatite bone cements after drying the constructs. The effect of concentration, immersion in PBS, and post-printing processes like sintering (1100°C, 3 hours). (n=5).

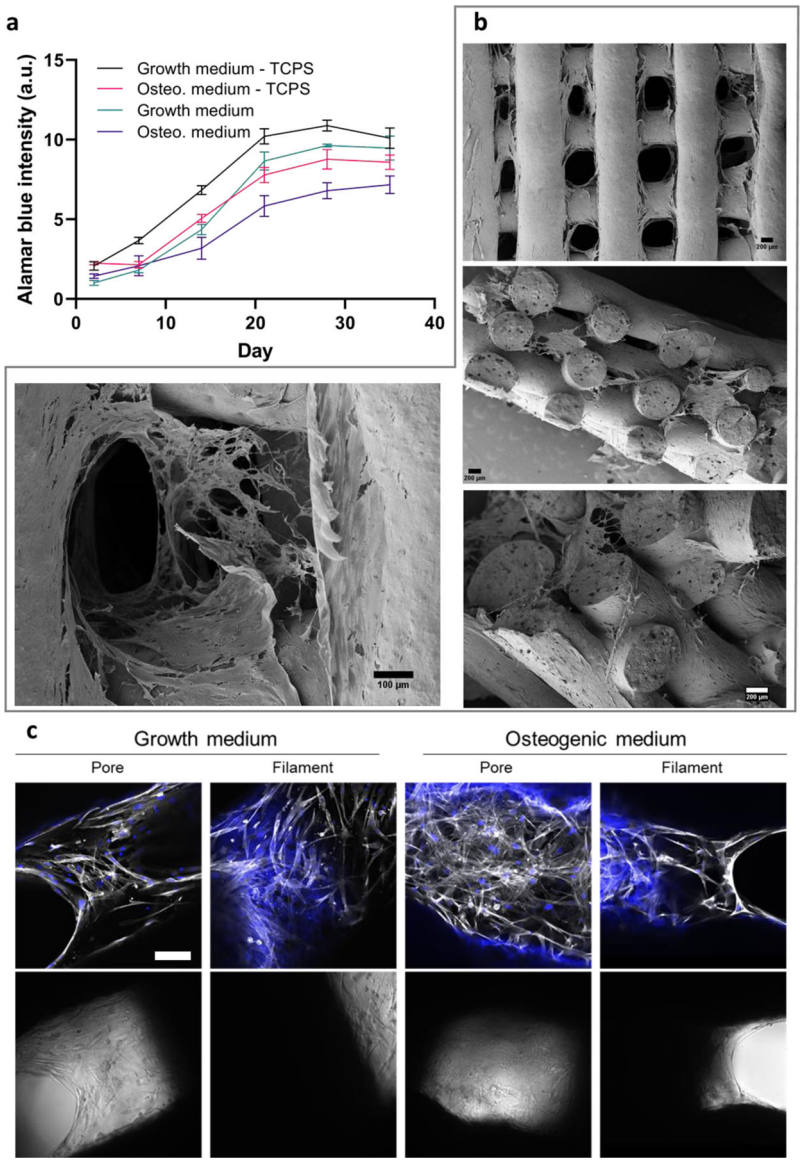

Figure 2:

Cytocompatibility of the 3D printed silk/HAP constructs. (a) alamarBlue (n=9) of hMSCs on 3D printed constructs and on tissue culture polystyrene, in growth and osteogenic media, for 35 days. (b-c) Scanning electron micrograph (b), confocal microscopy (c, top) and brightfield microscopy (c, bottom) of hMSCs on 3D printed constructs after 35 days of culture in growth medium, showing cell coverage and adhesion to the constructs, and growth of cells in the pores and between the filaments. Blue: nuclei (DAPI); White: actin cytoskeleton (Phalloidin-488). Scale bar: 100 µm.

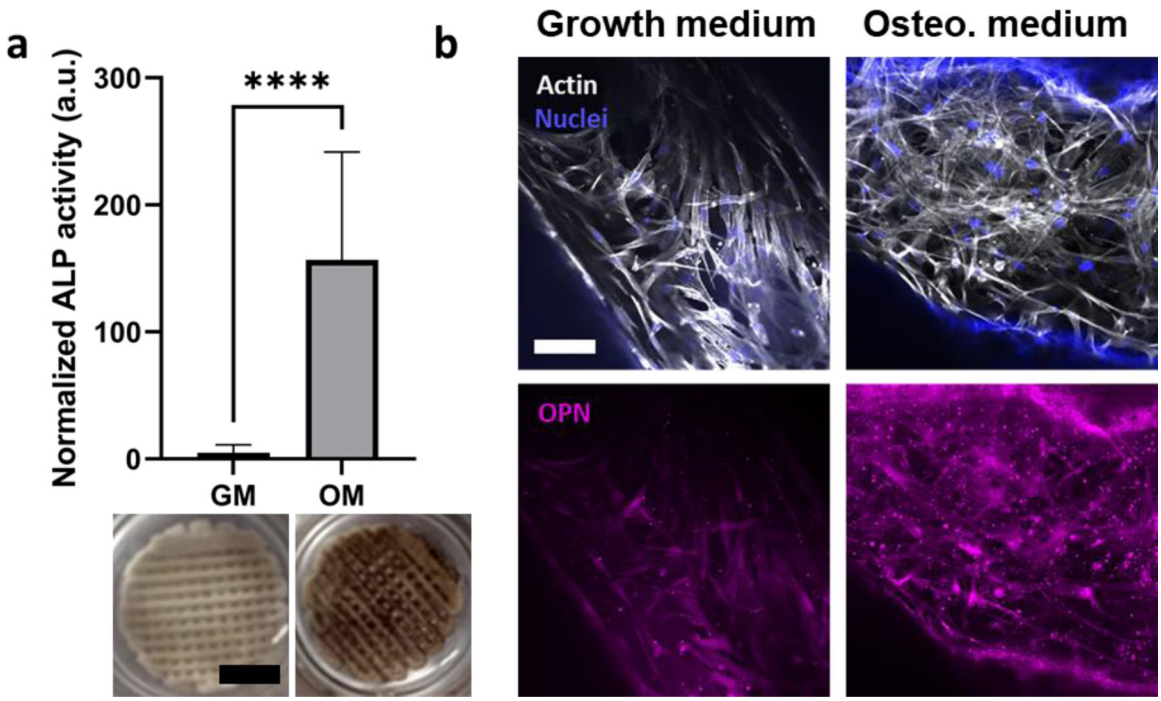

Figure 3:

Osteoconductivity of the 3D printed structures. (a) Activity of the enzyme alkaline phosphatase (ALP) in hMSCs after 21 days of culture in growth or osteogenic medium, normalized to the protein content (top). Staining for ALP in hMSCs after 21 days of culture in growth (left) or osteogenic (right) medium (bottom, scale bar: 5 mm). (b) Immunofluorescent staining of osteoblastic differentiation marker osteopontin (OPN, in magenta), showing the increase in OPN expression in osteogenic medium. For reference, the nuclei (blue, DAPI) and actin cytoskeleton (white, Phalloidin-488) are shown in the top panels. Scale bar: 100 μm.

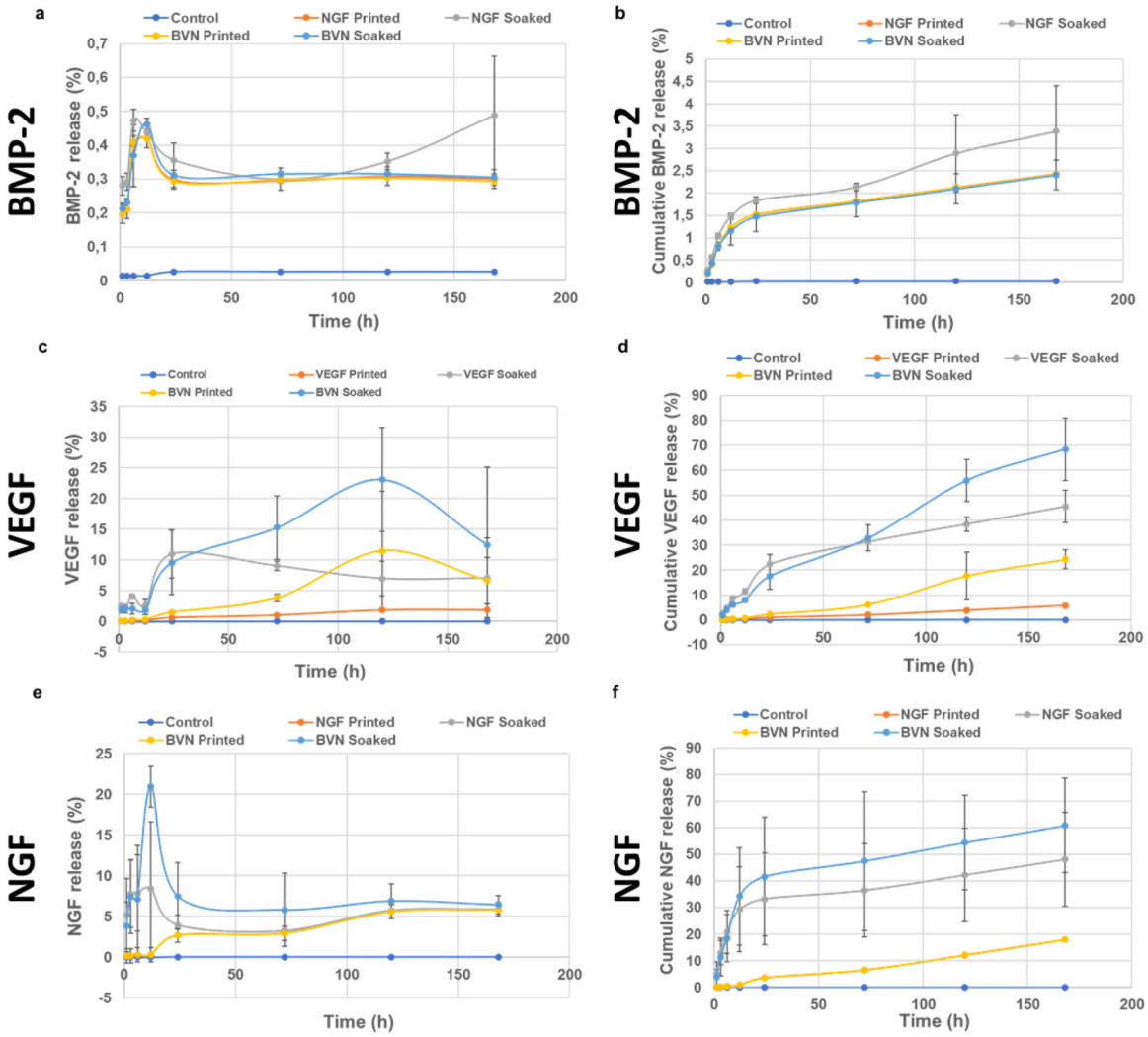

Figure 4.

Release of factors loaded into silk-Hap scaffolds. BMP-2 (a), VEGF (c) and NGF (e) release over time calculated as percent of the original amount loaded for the single factors (BMP-2/VEGF/NGF) and the triple factor (BVN) for printed and soaked samples. Cumulative release of BMP-2(b), VEGF (d) and NGF (f) release over time calculated as percent of the original amount loaded for the single factor (BMP-2/VEGF/NGF) and the triple factor (BVN) for printed and soaked samples. Data represent mean ± SD (n=5).

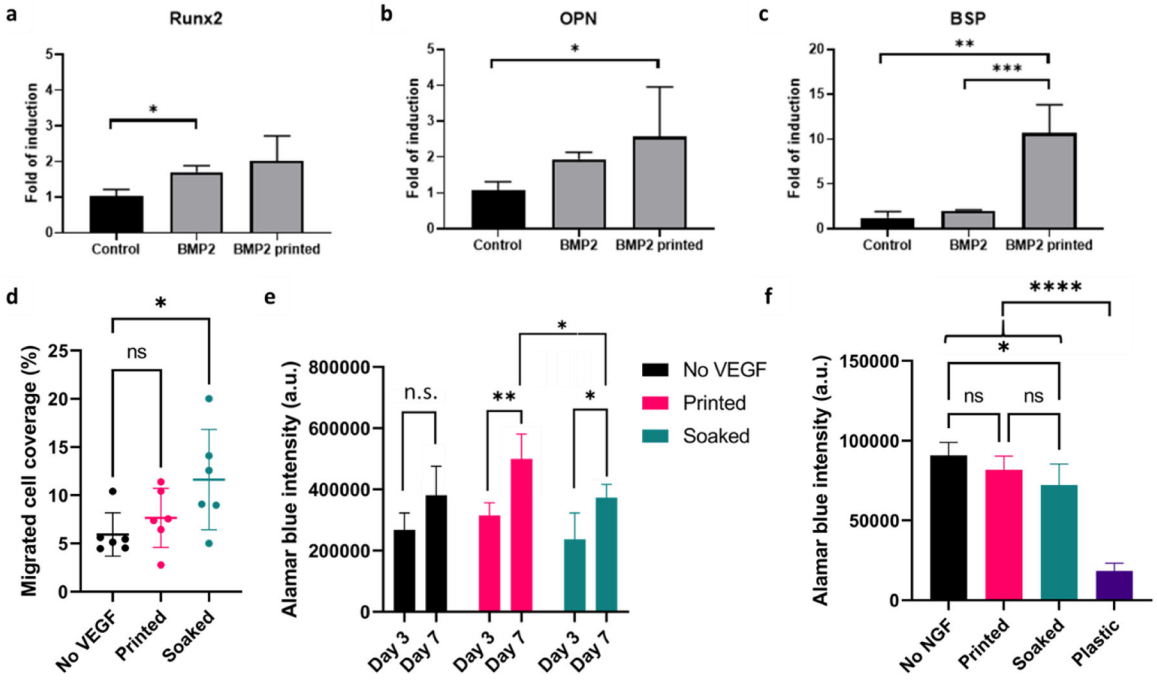

Figure 5:

Gene expression of Runx2 (a), OPN (b), and BSP (c) markers of hMSCs seeded for 7 days on silk scaffolds in the absence of additional growth factors (control), or loaded with morphogenic factor BMP2 after (BMP2) or before the printing process (BMP2 printed). Data represents mean ± SE (n=3–5) *: p˂0.05; **: p ˂0.01; ***: p ˂0.001. (d) Coverage of the bottom of the transwell (DAPI staining) after 3 hours in culture, showing estimation of HUVEC migration. (e) alamarBlue intensity of HUVECs on 3D printed constructs after 3 and 7 days of culture (n=6). (f) alamarBlue intensity of hiNSCs on 3D printed constructs after 7 days of culture (n=6).

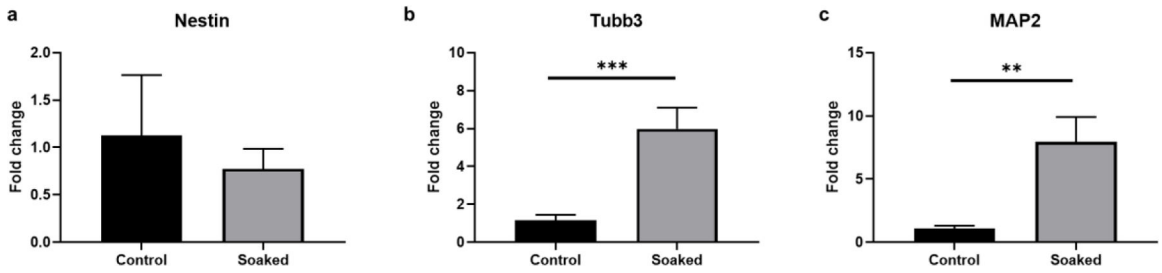

Figure 6:

Gene expression of Nestin (a), Tubulin β3 (Tubb3) (b), and Microtubule Associated Protein 2 (MAP2) (c) markers of NSCs (Nestin) and differentiated neurons (Tubb3 and MAP2) seeded for 3 days on silk scaffolds in the absence of additional growth factors (control) or loaded with NGF after the 3D-printing process (Soaked). Data represents mean ± SE (n=3–5) **: p ˂0.01; ***: p ˂0.001.

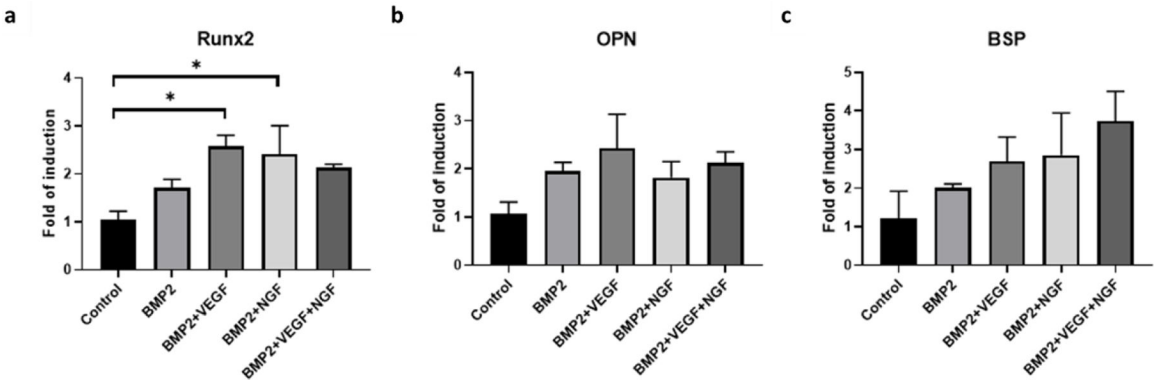

Figure 7:

Gene expression of Runx2 (a), OP (b), and BSP (c) markers of hMSCs seeded for 7 days on silk scaffolds in the absence of additional growth factors (control), or loaded with BMP2 (BMP), BMP2 and VEGF (BMP2+VEGF), BMP2 and NGF (BMP2+NGF) and BMP2, VEGF and NGF (BMP2+VEGF+NGF). Data represents mean ± SE (n=3–5) *: p ˂0.05; **: p ˂0.01; ***: p ˂0.001.

Table 1.

Primers used for Real-Time quantitative PCR. GAPDH, glyceraldehyde 3-phosphate dehydrogenase; Runx2, Runt-related transcription factor 2; OP, osteopontin; BSP, Bone Sialoprotein; Tubb3, Tubulin β3 Class III; MAP2, Microtubule Associated Protein 2.

Primer	Sequence (5'−3')	Tm (°C)
GAPDH	F- ACCCAGAAGACTGTGGATGG R- CAGTGAGCTTCCCGTTCAG	60
Runx-2	F- ATGCTTCATTCGCCTCAC R- ACTGCTTGCAGCCTTAAAT	60
OP	F- ATGAGAGCCCTCACACTCCTCG R- GTCAGCCAACTCGTCACAGTCC	60
BSP	F- ATGGCCTGTGCTTTCTCAATG R- GGATAAAAGTAGGCATGCTTG	60
Nestin	F- CTGCTACCCTTGAGACACCTG R- GGGCTCTGATCTCTGCATCTAC	60
Tubb3	F- GGCCAAGGGTCACTACACG R- GCAGTCGCAGTTTTCACACTC	60
MAP2	F- TGGTGCCGAGTGAGAAGAAG R- AGTGGTTGGTTAATAAGCCGAAG	60